ENGINEERING

Poro-elasto-capillary wicking of cellulose sponges

Jonghyun Ha,[1] Jungchul Kim,[2] Yeonsu Jung,[1] Giseok Yun,[1] Do-Nyun Kim,[1] Ho-Young Kim[1]*

We mundanely observe cellulose (kitchen) sponges swell while absorbing water. Fluid flows in deformable porous media, such as soils and hydrogels, are classically described on the basis of the theories of Darcy and poroelasticity, where the expansion of media arises due to increased pore pressure. However, the situation is qualitatively different in cellulosic porous materials like sponges because the pore expansion is driven by wetting of the surrounding cellulose walls rather than by increase of the internal pore pressure. We address a seemingly so simple but hitherto unanswered question of how fast water wicks into the swelling sponge. Our experiments uncover a power law of the wicking height versus time distinct from that for nonswelling materials. The observation using environmental scanning electron microscopy reveals the coalescence of microscale wall pores with wetting, which allows us to build a mathematical model for pore size evolution and the consequent wicking dynamics. Our study sheds light on the physics of water absorption in hygroscopically responsive multiscale porous materials, which have far more implications than everyday activities (for example, cleaning, writing, and painting) carried out with cellulosic materials (paper and sponge), including absorbent hygiene products, biomedical cell cultures, building safety, and cooking.

INTRODUCTION

As a major constituent of plants, cellulose has been used as a source of energy (*1*), food (*2*, *3*), building materials (*4*, *5*), clothing (*6*), and hygiene products (*7*) throughout human history. In particular, transfer and preservation of information has relied on wetting of cellulosic materials for millennia, beginning with papyrus in 3000 BCE. Porous materials made of cellulose still abound around us as paper and sponges, among many others (*8*, *9*). When we bring a dry paper or sponge into contact with water or ink, it absorbs the liquid while swelling simultaneously. Cellulose is a polymer whose chains are linked via a hydrogen bonding, and water molecules participate in the binding sites, causing the polymer volume to increase. Such physicochemical interaction of water and porous structure is called hygroscopic expansion, a mundane process observed in cleaning (*10*), painting (*11*), and writing (*12*).

Capillary imbibition of liquid in porous media (*12*–*15*) is described by Darcy's law, which gives the flow rate, $\mathbf{q}$, as a function of the permeability k and gradient of driving pressure ∇p: $\mathbf{q} = -(k/\mu)\nabla p$, where μ is the liquid viscosity. Because the permeability and the driving capillary pressure are respectively scaled as the cross-sectional area of the fluid conduit and the meniscus curvature at the wetting front, both of them are determined by the pore size. When the porous structure deforms due to liquid infiltration, the poroelastic theory gives the pore size and the flow rate in general. The theory is built upon the basic assumption that the pore pressure increases with the water content, the amount of liquid inside the void, which in turn causes the pore to swell (*16*). It has successfully described the behavior of liquids in many porous media, such as soil (*17*), sandstone (*18*), and hydrogel (*19*). However, the present problem of wicking and hygroexpansion defies such classical theoretical understanding for the following reason. As water progressively wets the cellulose materials, the macroscale pores at the spreading front expand due to swelling of the surrounding walls or scaffolds, not by increased pore pressure. The pore pressure should rather decrease because of volume expansion. This disobeys the fundamental framework of poroelastic theory, and thus, a completely different approach should be devised to understand the hygroscopic expansion of cellulosic porous materials containing macro voids.

[1]Department of Mechanical and Aerospace Engineering, Seoul National University, Seoul 08826, Korea. [2]Department of Extreme Thermal Systems, Korea Institute of Machinery and Materials, Daejeon 34103, Korea.
*Corresponding author: hyk@snu.ac.kr

RESULTS

Characteristics of cellulose sponges

As a model system to study this problem, we bring a commercial cellulose sponge (VWR) into contact with water or various liquids (table S1) and observe the liquid front rise against gravity (Fig. 1A). When using aqueous liquids, the sponge swells while being wetted. Plotting the rise height h versus time t (Fig. 1B) reveals that the power laws of h versus t differ in the early (filled symbols) and late (empty symbols) stages. Here, the heights are scaled by h_J, Jurin's height (*20*), a characteristic rise height at which the gravitational and capillary forces for a macropore are balanced: $h_J = \gamma/(\rho g R)$, with γ, ρ, and g being the liquid-air surface tension coefficient, the liquid density, and the gravitational acceleration, respectively. Figure 1C shows that the transition height at which the power law changes from $h \sim t^{1/2}$ (filled symbols) to $h \sim t^{1/5}$ (empty symbols) corresponds to Jurin's height of macro voids. Rationalizing these power laws allows us to understand the fundamental wicking dynamics of the hygroexpansive, heterogeneous porous materials.

We begin with characterizing the pore structure of the cellulose sponge. As shown in the scanning electron microscopy (SEM) images (Fig. 2, A to C), it consists of numerous cellulose sheets with two-dimensional microscale pores surrounding macro voids (*13*). The sheets approximately 10 nm in thickness are randomly stacked with nanometric spacings. Measuring the size distribution of the pores, we find the average radii of macro and micro voids to be $R = 0.73$ mm and $r_0 = 4$ μm, respectively (fig. S1). Pores finer than the micrometric voids are hardly found in the sheets.

Capillary flows and volumetric expansion in porous media

Darcy's law gives the wicking velocity u in a porous medium, which we now write as $u = -(k/\mu)dp/dz$. The driving pressure arises as a consequence of capillary action so that $\Delta p \sim \gamma/\lambda$, where $\sim$ signifies "is scaled as" and λ is the radius of curvature of the front meniscus. The permeability k is scaled as the cross-sectional area of fluid conduit, over which the viscous stress resisting the fluid flow develops. Noting that h measures the distance from the free surface of the liquid reservoir to the wet front, u and $\dot{h} = dh/dt$ can differ when the media volume changes. For the isotropically expanding materials like cellulose sponges as shown in Fig. 3D, the bottom of the sponge descends by $h\varepsilon_s$, with ε_s being the hygroscopic strain of the saturated sponge, so that the total wet distance $H \approx h(1 + \varepsilon_s)$. Not all the liquid flowing

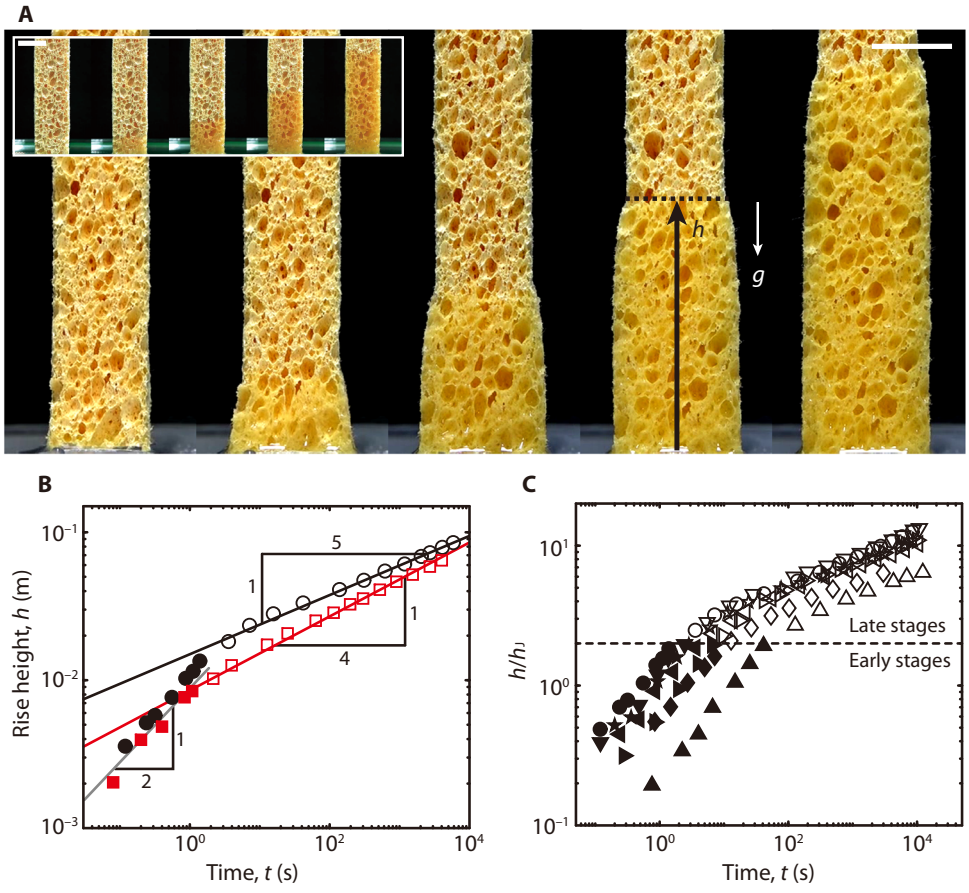

Fig. 1. Capillary rise in cellulose sponges. (**A**) Optical images for wicking of water (main panel) and turpentine (inset) in the initially dry sponge. The sponge swells when contacting water or aqueous liquids (movie S1). From left to right, t = 0, 1, 10, 100, 1000 s. Scale bar, 10 mm. (**B**) Experimentally measured rise height of water (black symbols) and turpentine (red symbols) versus time. In the early stages (filled symbols), the rise height grows like $t^{1/2}$ (gray line) for both the liquids. In the late stages (open symbols), the rise height of water follows the $t^{1/5}$ rule (black line), whereas that of turpentine behaves like $t^{1/4}$ (red line). (**C**) The power law of the height changes when the rise height h reaches Jurin's height of macropores: $h_J = \gamma/(\rho g R)$, so the transition occurs at $h/h_J \sim 1$. The symbols for different liquids are listed in table S1. All the experimental data for the rise height are the average of three measurements, with the error bars smaller than the size of symbols.

into the sponge contributes to the rise of H because of the transverse expansion of the sponge, leading us to write $\dot{H} \approx u/(1+\varepsilon_s)^2$ (section S1). The hygroscopic strain of the used sponge is at most 0.23, allowing us to neglect higher-order terms of ε_s. Because $h \approx H/(1+\varepsilon_s)$, we get $\dot{h} \approx u/\zeta$, with $\zeta \approx 1 + 3\varepsilon_s$ being the coefficient of volumetric expansion.

When the macro voids are completely filled with infiltrating liquid, as observed for the early stages of capillary rise (Fig. 3, A and C), $\lambda \sim R$ and $k \sim R^2$. Then, we get $\dot{h} \sim \gamma R/(\zeta\mu h)$ so that $h \sim [\gamma R t/(\zeta\mu)]^{1/2}$, which is consistent with Lucas-Washburn's rule (*21*, *22*) except the fact that the effect of swelling (ζ) is included. We plot the rise heights of Fig. 4A according to our scaling law to find the scattered data to collapse onto a single straight line in Fig. 4B together with the data of nonaqueous liquids ($\varepsilon_s = 0$). When plotting h versus $\gamma Rt/\mu$ without ζ in Fig. 4C, we find two distinct lines depending on whether the sponge swells or not.

Darcy's law for late stages

Beyond Jurin's height, macro voids cannot be completely filled because the capillary pressure based on the void radius cannot withstand the hydrostatic pressure. Then, the foregoing model fails (*13*), which is consistent with the change of the slopes in Fig. 1B. In this regime, the rise is rather driven by the capillary pressure provided by the micropores of characteristic radius r so that $\lambda \sim r$. However, the liquid does not flow only through microporous sheets, but it can also wet the corners of macro voids in such a way that the radius of corner meniscus δ balances capillary and hydrostatic pressure: $\gamma/\delta \sim \rho g h$. We display the image of the macro void partially filled with liquid and its schematic in Fig. 3 (A and B). Because the liquid that advances the wetting front can be supplied from the wet corners rather than the network of micropores owing to reduced viscous stress (for $\delta >> r$) as shown in the box of Fig. 3D, we should take the permeability k as the cross-sectional area of the wet corner. A simple geometric consideration allows us to write the area as δ^2 so that $k \sim \delta^2$. Then, Darcy's law, $u \sim \delta^2\gamma/(\mu r h)$, gives

$$u \sim \frac{\gamma^3}{\mu(\rho g)^2 r h^3} \quad (1)$$

Pore growth due to hygroscopic swelling

When the micropore size is invariant as $r = r_0$, we easily get $h \sim t^{1/4}$, which was shown to hold for the rise of nonaqueous liquids without causing hygroscopic swelling (*13*). However, in case of water wicking, we have discovered drastic shape changes of micropores in an environmental SEM (ESEM) chamber, where the RH around a sponge specimen has increased from 10 to 100%. See Fig. 2D and

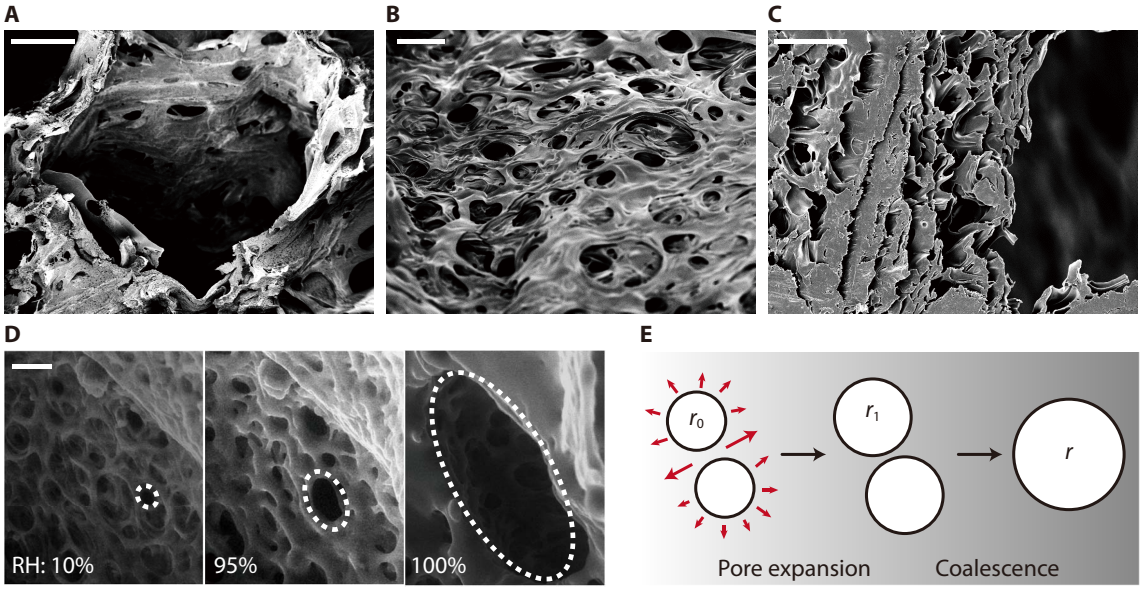

Fig. 2. Microscopic images of the cellulose sponge. SEM images of macropores (**A**), micropores (**B**), and cross section of the sheets (**C**). Scale bars, 300 μm (A) and 10 μm (B and C). (**D**) Merging of micropores due to hygroscopic expansion of the cellulose sheet, as imaged by ESEM. The pores start to grow when the relative humidity (RH) exceeds 90%, and they coalesce with their neighbors. Scale bar, 10 μm. (**E**) Schematic illustration of micropore expansion and coalescence. The micropores grow from r_0 to r_1 in radius (pore expansion) and then merge to form large micropores of radius r (coalescence).

movie S2 for experimental images and Materials and Methods for experimental procedure. The expansion process of the porous sheet can be decomposed into two steps (Fig. 2E). First, the pore size grows from r_0 to r_1, allowing us to write $r_1 \sim r_0(1 + \varepsilon)$. As the expanded pores get closer, they merge to form large pores of radius r accompanied by the decrease of the number of pores from N_0 to N. Because of the insignificant change of the total area of pores upon coalescence, we get $N_0 r_1^2 \sim N r^2$. Similar growth and coalescence of pores can be easily observed by stretching a macroscopic perforated polymer film as well as in microscopic ductile fracture (*23*) and polymer crack (*24*). The ratio $N_0/N > 1$ should increase with ε, which we simply estimate as $N_0/N \sim 1 + \beta\varepsilon$ (section S2 and figs. S1 to S4). The prefactor β is a function of a distribution of interpore distances, and a detailed discussion of the estimate is given in section S2. With the measured values of $\beta \approx 50$ and $\varepsilon \sim \varepsilon_s \approx 0.23$ in the cellulose sponges, we obtain $N_0/N \sim \beta\varepsilon$, and thus, $r \sim (\beta\varepsilon)^{1/2} r_0$. When the wet sponges are dried, a similar size distribution of micropores to the originally dry state is recovered (section S3 and fig. S5).

Hygroscopic swelling in cellulose sheets

The degree of hygroscopic expansion of a porous sheet as the wetting front propagates is related to the amount of water absorbed in the sheet. See fig. S6 (section S4) for the schematic of the porous cellulose sheet being wetted. The hygroscopic strain $\varepsilon = \alpha\eta$, where α is the hygroscopic swelling coefficient measured to be $\alpha \approx 0.33$ (section S5 and fig. S7). The volume fraction of aqueous liquid, η, in the front sheet is given by $\eta = V_l/V_c$, with V_l and V_c being the volume of liquid and of cellulose, respectively. Because a liquid is absorbed into a sheet of thickness s by the distance l_d, $V_l \sim N_0 r_0 l_d s$. The diffusion length l_d is scaled as $l_d \sim (D\tau)^{1/2}$, with τ being the characteristic time taken for the rising liquid to pass the sheet: $\tau \sim s/u$. The diffusivity of a dense hygroscopic medium (*19*), D, is given by $D = 2Gk_c(1 - \nu)/(1 - 2\nu)/\mu$, where the shear modulus G = 1.62 MPa (section S6 and fig. S8), the permeability $k_c \sim r_c^2/32$, with r_c being the typical pore radius (order of 1 nm) of a cellulose sheet (*25*), and Poisson's ratio $\nu = 0.3$ (*26*). The cellulose volume $V_c \sim N_0 r_0^2 s(1 - \phi)/\phi$, where the porosity ϕ is the ratio of the micropore volume to the total sheet volume (section S4 and fig. S6).

Although the moisture diffusion at the wetting front determines the size of newly wetted pores, the diffusion length itself is insignificant as compared with the overall rise height. Namely, we find that the typical increment of the diffusion length Δl_d is much smaller than that of the rise height Δh, to give $\Delta l_d/\Delta h \sim 0.01$ for a given duration even in the late stages.

Dynamics of wicking and swelling in late stages

The foregoing considerations allow us to write ε as $\varepsilon \sim \alpha(Ds/u)^{1/2}\phi/(1-\phi)/r_0$, which leads to

$$r \sim \left(\frac{\alpha\beta\phi r_0}{1-\phi}\right)^{1/2} (Ds)^{1/4} u^{-1/4} \tag{2}$$

The relation indicates that the micropore radius at the wet front increases as the liquid rising velocity (u) decreases, which results in the decrease in the capillary pressure ($\sim\gamma/r$). Combining Eqs. 1 and 2 and recalling $\dot{h} \approx u/\zeta$, we obtain a power law for the rise height in the late stages, $h \sim (Bt)^{1/5}$, with B given by

$$B = \frac{1}{\zeta}\left[\frac{\gamma^3(1-\phi)^{1/2}}{\mu(\rho g)^2(\alpha\beta\phi r_0)^{1/2}(Ds)^{1/4}}\right]^{4/3} \tag{3}$$

We plot the experimental results in the late stages of Fig. 4D according to scaling law (Eq. 3) in Fig. 4E. We see that the experimental data for various liquids are collapsed onto a single master curve despite the variations of γ, μ, ρ, and D, consistent with our theory. Figure 4F plots h based on the scaling law suggested for nonswelling sponges (*13*): $h \sim \{\gamma^3 t/[\mu(\rho g)^2 r_0]\}^{1/4}$. Although the data

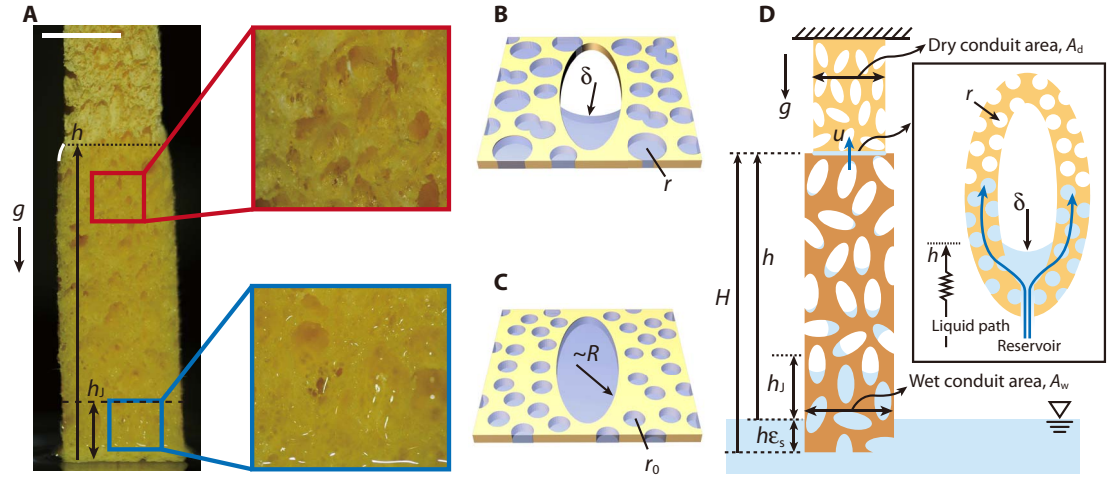

Fig. 3. The difference of wicking behavior between early and late stages. (**A**) Optical image of a sponge wetted by water. At small h, or in the early stages, the macro voids are completely filled with liquid. However, at large h, or in the late stages, they are only partially filled with liquid. A white curved line indicates the deformation of sponge due to the constraint of the dry upper part (section S1). The blue and red boxes show macro voids completely and partially filled with liquid, respectively. Scale bar, 10 mm. (**B**) Schematic of liquid-filling behavior in the late stages. Macro voids are not completely filled with liquid due to gravitational effects, whereas micropores are fully occupied with liquid. The radius of curvature δ of the meniscus in the macro void is determined by the balance between gravitational and capillary forces: $δ \sim γ/(ρgh)$. (**C**) Schematic of a macro void of radius R in a microporous sheet in the early stages. Both macro and micro voids are completely filled with liquid. (**D**) Simplified model of the sponge whose wetting behavior is mathematically analyzed. Black box shows the liquid path near the wetting front. The liquid permeates into micropores from the wet corner of macropores.

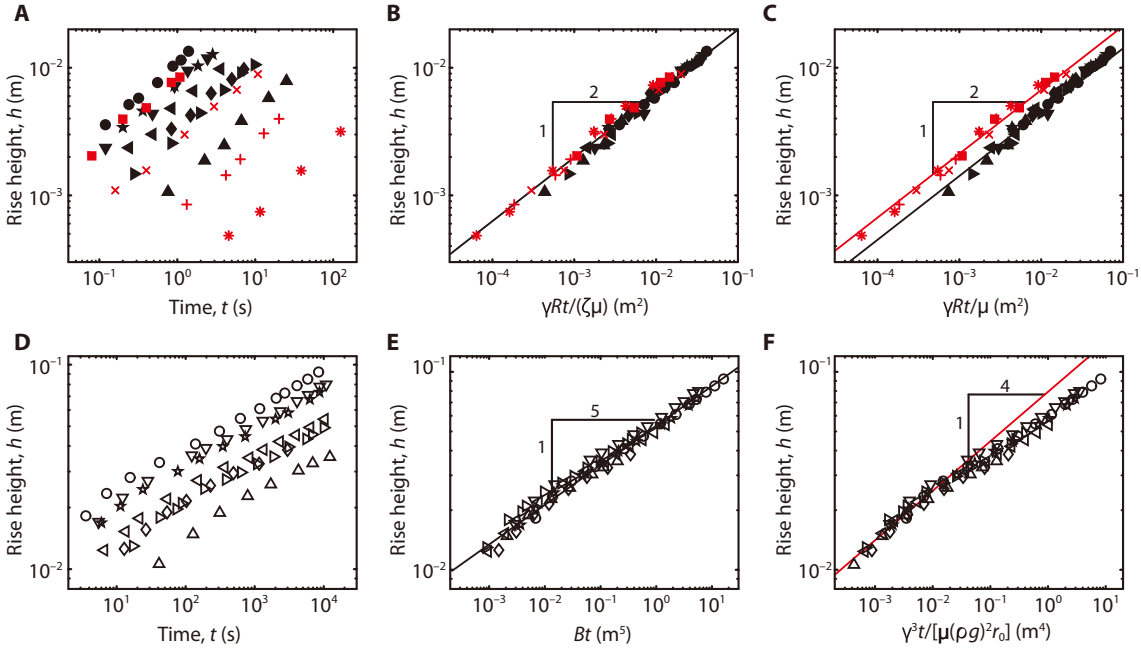

Fig. 4. Wicking dynamics in different stages. (**A**) Experimentally measured rise height versus time in the early stages. (**B**) The early-stage data are collapsed onto a single line when plotted according to our scaling law $h \sim [γRt/(ζμ)]^{1/2}$. The law holds for both the aqueous and nonaqueous liquids. (**C**) Two collapsed lines for aqueous (black line) and nonaqueous liquids (red line). (**D**) Experimentally measured rise height of aqueous liquids versus time in the late stages. (**E**) The late-stage data are collapsed onto a single line when plotted against our scaling law $h \sim (Bt)^{1/5}$. (**F**) The experimental results appear to collapse onto a single line but disobey the $t^{1/4}$ rule (Eq. 1). The symbols for different liquids are listed in table S1.

appear to collapse onto a single line, h does not follow $h \sim t^{1/4}$, invalidating the nonswelling theory for the current situation. We show in section S7 (fig. S9) that even with aqueous liquids, the rise height follows the $t^{1/4}$ law in the late stages for the sponges that have been pre-wetted and fully swollen in advance.

DISCUSSION

We have constructed the theoretical framework to analyze the liquid flow in hygroexpansive porous medium, where multiscale pore dynamics cannot be adequately accounted for by conventional poroelasticity theory. In particular, our analysis correctly captures the $t^{1/5}$ behavior of

the rise height in the late stages by considering the expansion of micropores as a function of the liquid rise speed, which determines the diffusion length within a cellulose sheet. Although the evaporation of water from the wet sponge occurs in the course of capillary rise, it has been ignored in our analysis because its rate ($q \approx 6 \times 10^{-9}$ m/s as experimentally measured) is negligibly small compared with the typical wicking velocity $u \sim 10^{-4}$ m/s in the late stages. We note that although cellulose is a major constituent of wood, the porous structure of artificially manufactured cellulose sponges is distinguished from wood that has grown in nature. One of those remarkable differences is that wood has submicrometric pores in a hierarchical order (*25*), which are invisible in the cellulose sponges.

Besides cellulose sponges, a variety of mundane and industrial materials of heterogeneous porosity can benefit from our theory, including biomedical devices such as the cytosponge (*27*), cell cultures (*28*), shape-morphing microneedles (*29*), soft actuators (*30*, *31*), and plant seeds (*32*). Paper itself involves only microscale pores (*33*, *34*), but crumpled or folded paper forms macro voids, wetting of which should be in line with the current problem. In addition to cellulosic porous materials, hygroexpansive porous bread composed of starch (*35*) was found to exhibit micropore coalescence and to follow the $t^{1/5}$ law in the late stages of vertical wicking (section S8 and fig. S10). This enables us to start thinking about applying our theoretical framework to a relevant field in the science of cooking. Although we have concentrated on the power-law behavior of liquid dynamics, hygroscopic deformation dynamics of the heterogeneous porous solid structure would help us to fully understand and control the soft materials of ever-growing importance.

MATERIALS AND METHODS

Experimental procedures of ESEM

In the ESEM chamber (XL-30 FEG, Philips), we placed a piece of cellulose sponge, $5 \times 5 \times 1$ mm^3 in volume, on a Peltier plate, which was kept at 2°C. Water vapor was supplied into the chamber to increase the RH. The sponge underwent drastic shape change as the environmental humidity reached approximately 90% by absorbing water molecules. The deformation of the sponge was insignificant when RH was below 90%, indicating that water molecules hardly infiltrate the sponge until the vapor pressure reaches a critical value. The imaging results are shown in Fig. 2D.

SUPPLEMENTARY MATERIALS

Supplementary material for this article is available at http://advances.sciencemag.org/cgi/content/full/4/3/eaao7051/DC1

section S1. Effects of isotropic volumetric expansion on liquid rise height
section S2. Correlation between hygroscopic strain and pore coalescence
section S3. Recovery of microporous structure of cellulose sponges
section S4. The volume fraction of aqueous liquid in a cellulose sheet
section S5. Effects of water concentration on hygroscopic strain
section S6. Mechanical properties of cellulose sponges
section S7. Capillary rise in pre-swollen sponges
section S8. Scaling laws of water rise within bread made from starch
fig. S1. The measurement data of the cellulose sponge structure.
fig. S2. Macroscopic experiments for pore coalescence.
fig. S3. Numerical analysis of porous sheet deformation.
fig. S4. Moisture flux into cellulose sheet in ESEM chamber.
fig. S5. Microporous structure of cellulose sponges after cycles of wetting and drying with water.
fig. S6. Analysis of the cellulose sheets.
fig. S7. Hygroscopic strain of saturated sponge for different water contents in aqueous glycerin and ethylene glycol.
fig. S8. Shear modulus of dry and wet cellulose sponge.
fig. S9. Capillary rise height of water versus time in an initially dry sponge (black) and pre-swollen sponge (red).
fig. S10. Capillary rise in porous bread.
table S1. List of liquid properties and symbols.
movie S1. Wicking and swelling in the cellulose sponge.
movie S2. The merging of micropores in the cellulose sheets.
References (*36*–*38*)

REFERENCES AND NOTES

1. R. C. Saxena, D. K. Adhikari, H. B. Goyal, Biomass-based energy fuel through biochemical routes: A review. *Renew. Sust. Energ. Rev.* **13**, 167–178 (2009).
2. M. A. García, C. Ferrero, N. Bértola, M. Martino, N. Zaritzky, Edible coatings from cellulose derivatives to reduce oil uptake in fried products. *Innov. Food Sci. Emerg. Technol.* **3**, 391–397 (2002).
3. J. F. Ang, Water retention capacity and viscosity effect of powdered cellulose. *J. Food Sci.* **56**, 1682–1684 (1991).
4. S. Goodhew, R. Griffiths, Sustainable earth walls to meet the building regulations. *Energ. Buildings* **37**, 451–459 (2005).
5. A. K. Bledzki, J. Gassan, Composites reinforced with cellulose based fibres. *Prog. Polym. Sci.* **24**, 221–274 (1999).
6. S. B. Stanković, D. Popović, G. B. Poparić, Thermal properties of textile fabrics made of natural and regenerated cellulose fibers. *Polym. Test.* **27**, 41–48 (2008).
7. P. C. K. Sankar, R. Ramakrishnan, M. J. Rosemary, Biological evaluation of nanosilver incorporated cellulose pulp for hygiene products. *Mater. Sci. Eng. C Mater. Biol. Appl.* **61**, 631–637 (2016).
8. Z. Weng, Y. Su, D.-W. Wang, F. Li, J. Du, H.-M. Cheng, Graphene–cellulose paper flexible supercapacitors. *Adv. Energy Mater.* **1**, 917–922 (2011).
9. M. Märtson, J. Viljanto, T. Hurme, P. Laippala, P. Saukko, Is cellulose sponge degradable or stable as implantation material? An in vivo subcutaneous study in rat. *Biomaterials* **20**, 1989–1995 (1999).
10. S. T. Nguyen, J. Feng, N. T. Le, A. T. T. Le, N. Hoang, V. B. C. Tan, H. M. Duong, Cellulose aerogel from paper waste for crude oil spill cleaning. *Ind. Eng. Chem. Res.* **52**, 18386–18391 (2013).
11. S. Capodicasa, S. Fedi, A. M. Porcelli, D. Zannoni, The microbial community dwelling on a biodeteriorated 16th century painting. *Int. Biodeter. Biodegr.* **64**, 727–733 (2010).
12. J. Kim, M.-W. Moon, K.-R. Lee, L. Mahadevan, H.-Y. Kim, Hydrodynamics of writing with ink. *Phys. Rev. Lett.* **107**, 264501 (2011).
13. J. Kim, J. Ha, H.-Y. Kim, Capillary rise of non-aqueous liquids in cellulose sponges. *J. Fluid Mech.* **818**, R2 (2017).
14. S. J. Kim, J. W. Choi, M.-W. Moon, K.-R. Lee, Y. S. Chang, D.-Y. Lee, H.-Y. Kim, Wicking and flooding of liquids on vertical porous sheets. *Phys. Fluids* **27**, 032105 (2015).
15. J. Kim, M.-W. Moon, H.-Y. Kim, Dynamics of hemiwicking. *J. Fluid Mech.* **800**, 57–71 (2016).
16. J. I. Siddique, D. M. Anderson, A. Bondarev, Capillary rise of a liquid into a deformable porous material. *Phys. Fluids* **21**, 013106 (2009).
17. M. A. Biot, General theory of three-dimensional consolidation. *J. Appl. Phys.* **12**, 155–164 (1941).
18. A. Nur, J. D. Byerlee, An exact effective stress law for elastic deformation of rock with fluids. *J. Geophys. Res.* **76**, 6414–6419 (1971).
19. J. Yoon, S. Cai, Z. Suo, R. C. Hayward, Poroelastic swelling kinetics of thin hydrogel layers: Comparison of theory and experiment. *Soft Matter* **6**, 6004–6012 (2010).
20. J. Jurin, An account of some experiments shown before the Royal Society; with an enquiry into the cause of the ascent and suspension of water in capillary tubes. *Philos. Trans.* **30**, 739–747 (1718).
21. R. Lucas, Ueber das Zeitgesetz des kapillaren Aufstiegs von Flüssigkeiten. *Kolloid Z.* **23**, 15–22 (1918).
22. E. W. Washburn, The dynamics of capillary flow. *Phys. Rev.* **17**, 273–283 (1921).
23. G. L. Roy, J. D. Embury, G. Edwards, M. F. Ashby, A model of ductile fracture based on the nucleation and growth of voids. *Acta Metall. Mater.* **29**, 1509–1522 (1981).
24. H. H. Kausch, Ph. Beguelin, M. Fischer, Failure of particulate reinforced polymers. *Mech. Compos. Mater.* **36**, 177–184 (2000).
25. D. Klemm, B. Heublein, H.-P. Fink, A. Bohn, Cellulose: Fascinating biopolymer and sustainable raw material. *Angew. Chem. Int. Ed. Engl.* **44**, 3358–3393 (2005).
26. R. J. Roberts, R. C. Rowe, P. York, The Poisson's ratio of microcrystalline cellulose. *Int. J. Pharm.* **105**, 177–180 (1994).
27. P. Lao-Sirieix, R. C. Fitzgerald, Screening for oesophageal cancer. *Nat. Rev. Clin. Oncol.* **9**, 278–287 (2012).
28. M. Bhattacharya, M. M. Malinen, P. Lauren, Y.-R. Lou, S. W. Kuisma, L. Kanninen, M. Lille, A. Corlu, C. GuGuen-Guillouzo, O. Ikkala, A. Laukkanen, A. Urtti, M. Yliperttula,

Nanofibrillar cellulose hydrogel promotes three-dimensional liver cell culture. *J. Control. Release* **164**, 291–298 (2012).
29. S. Y. Yang, E. D. O'Cearbhaill, G. C. Sisk, K. M. Park, W. K. Cho, M. Villiger, B. E. Bouma, B. Pomahac, J. M. Karp, A bio-inspired swellable microneedle adhesive for mechanical interlocking with tissue. *Nat. Commun.* **4**, 1702 (2013).
30. J. Y. Chung, H. King, L. Mahadevan, Evaporative microclimate driven hygrometers and hygromotors. *Europhys. Lett.* **107**, 64002 (2014).
31. A. S. Gladman, E. A. Matsumoto, R. G. Nuzzo, L. Mahadevan, J. A. Lewis, Biomimetic 4D printing. *Nat. Mater.* **15**, 413–418 (2016).
32. W. Jung, W. Kim, H.-Y. Kim, Self-burial mechanics of hygroscopically responsive awns. *Integr. Comp. Biol.* **54**, 1034–1042 (2014).
33. E. Reyssat, L. Mahadevan, Hygromorphs: From pine cones to biomimetic bilayers. *J. R. Soc. Interface* **6**, 951–957 (2009).
34. M. Lee, S. Kim, H.-Y. Kim, L. Mahadevan, Bending and buckling of wet paper. *Phys. Fluids* **28**, 042101 (2016).
35. N. N. Hellman, T. F. Boesch, E. H. Melvin, Starch granule swelling in water vapor sorption. *J. Am. Chem. Soc.* **74**, 348–350 (1952).
36. J. Kováčik, Correlation between Young's modulus and porosity in porous materials. *J. Mater. Sci. Lett.* **18**, 1007–1010 (1999).
37. Glycerine Producers' Association, *Physical Properties of Glycerine and Its Solutions* (Glycerine Producers' Association, 1963).
38. Y. S. Won, D. K. Chung, A. F. Mills, Density, viscosity, surface tension, and carbon dioxide solubility and diffusivity of methanol, ethanol, aqueous propanol, and aqueous ethylene glycol at 25°C. *J. Chem. Eng. Data* **26**, 140–141 (1981).

Acknowledgments: We are grateful to L. Mahadevan for stimulating discussion. **Funding:** This work was supported by Samsung Research Funding and Incubation Center of Samsung Electronics (project no. SRFC-MA1301-05) and National Research Foundation of Korea (grant nos. 2016901290 and 2016913167) via SNU-IAMD. **Author contributions:** J.H. and J.K. carried out the experiments. J.H. and Y.J. analyzed the pore coalescence process. G.Y. and D.-N.K. performed numerical simulations. J.H. and H.-Y.K. developed the mathematical model and wrote the paper. H.-Y.K. conceived and supervised the project. **Competing interests:** The authors declare that they have no competing interests. **Data and materials availability:** All data needed to evaluate the conclusions in the paper are present in the paper and/or the Supplementary Materials. Additional data related to this paper may be requested from the authors.

Submitted 17 August 2017
Accepted 14 February 2018
Published 30 March 2018
10.1126/sciadv.aao7051

Citation: J. Ha, J. Kim, Y. Jung, G. Yun, D.-N. Kim, H.-Y. Kim, Poro-elasto-capillary wicking of cellulose sponges. *Sci. Adv.* **4**, eaao7051 (2018).

Science Advances

Poro-elasto-capillary wicking of cellulose sponges

Jonghyun Ha, Jungchul Kim, Yeonsu Jung, Giseok Yun, Do-Nyun Kim and Ho-Young Kim

Sci Adv **4** (3), eaao7051.
DOI: 10.1126/sciadv.aao7051

Science Advances

AAAS

advances.sciencemag.org/cgi/content/full/4/3/eaao7051/DC1

Supplementary Materials for

Poro-elasto-capillary wicking of cellulose sponges

Jonghyun Ha, Jungchul Kim, Yeonsu Jung, Giseok Yun, Do-Nyun Kim, Ho-Young Kim

Published 30 March 2018, *Sci. Adv.* **4**, eaao7051 (2018)
DOI: 10.1126/sciadv.aao7051

The PDF file includes:

Other Supplementary Material for this manuscript includes the following:

(available at advances.sciencemag.org/cgi/content/full/4/3/eaao7051/DC1)

- movie S1 (.mov format). Wicking and swelling in the cellulose sponge.
- movie S2 (.mov format). The merging of micropores in the cellulose sheets.

section S1. Effects of isotropic volumetric expansion on liquid rise height

The cellulose sponge swells isotropically by absorbing water or aqueous solutions, but it should match the size of the upper dry region near the wet-dry interface. The region of such deformation (white curved line in Fig. 3A of the main text), whose length is approximately 2 mm, is relatively small compared to the rise height h and Jurin's height h_J, which allows us to simplify the model as illustrated in Fig. 3D.

In the vertical direction, the total wet distance H from the bottom of the sponge to the wet front is related to the measured rise height h by $h = H/(1+\varepsilon_s)$. The liquid flux that enters the initially dry region of the cross-sectional area A_d, uA_d, contributes to the transverse expansion causing the area to increase from A_d to $A_w = A_d(1+\varepsilon_s)^2$ as well as to the rise of the wet front $\dot{H}$. Hence, we write $uA_d \approx \dot{H}A_w$, which leads to $\dot{H} \approx u/(1+\varepsilon_s)^2$.

section S2. Correlation between hygroscopic strain and pore coalescence

We consider a thin perforated sheet with N_0 pores, which is stretched isotropically in its plane. As demonstrated in movie S2 which actually employs a biaxial extension due to the limit of experimental setup, the growing holes approach each other until they merge to form a larger pore. We observe similar coalescence process of micropores in the cellulose sheet as it becomes wet in Fig. 2D of the main text. The similarity between the stretched perforated membrane and hygroscopically expanding porous sheet is discussed below. Our theory requires a simple relationship between the hygroscopic strain ε and the change of pore numbers via merging, or $N_0/N = f(\varepsilon)$ with N_0 and N being the number of pores before and after coalescence. Because the change of pore numbers via coalescence has been seldom treated theoretically, we employ an experimental approach to empirically find the functional form of $f(\varepsilon)$.

As shown in fig. S2A, we start with thin PDMS (polydimethylsiloxane) films 100 μm in thickness with dozens of holes of the radius a = 2 mm. We stretch the films in the two perpendicular directions using two linear stages (M-IMS300LM, Newport) as shown in fig. S2B and C. We count the number of pores as the strain increases to obtain N_0/N as a function of ε. The results are displayed in fig. S2D, where the number ratio linearly increases with ε once the strain reaches the threshold value. The value is different for each perforation condition, which also affects the slope of the straight lines. Although the hole radii were identical for all the films, their spacings were different. Figure S2E and F show the probability of the inter-pore distance d scaled by a for the two extreme cases, films 1 and 5. When the inter-pore distance is densely distributed in the range of very small values as in film 1, the threshold strain over which N_0/N begins to increase is close to zero and the increase rate (slope of the line) is large. For films with relatively large inter-pore distances as in film 5, the threshold strain is relatively large and the line slope is small.

Our measurement result of inter-pore distance of micropores in the cellulose sheet is displayed in fig. S1C. It clearly shows that the pores are rather densely spaced, so that the inter-pore distance probability resembles that of film 1 in fig. S2E. Therefore, we assume

$N_0/N \approx 1+ \beta\varepsilon$ for the cellulose sheet. We empirically find β based on the number of pores of a cellulose sheet before (N_0) and after (N) wetting in the ESEM chamber and the hygroscopic strain ($\varepsilon \approx 0.23$). As a result of three runs, we obtain $\beta \approx 50 \pm 7.7$, which further allows us to estimate $N_0/N \approx \beta\varepsilon$ for $\beta\varepsilon >> 1$.

While physical mechanisms causing stress and strain in stretched membranes and hygroscopically expanding sheets are different, the resultant deformation patterns are similar. To illustrate the similarity, we perform finite element analysis (FEA) for a circular sheet with two and four holes to compare the deformation patterns under tension and hygroscopic pore expansion using the commercial FEA program, ADINA version 9.3. Sheet stretching is simulated by imposing a radial force uniformly distributed along the outer boundary of the sheet (fig. S3A). To model the case of hygroscopic pore expansion, a thin circular layer of high moisture content is introduced near the pore boundary. This is a simple model for what happens in the actual wicking experiments, where the water that enters a micropore diffuses outward from the pore boundary while keeping the water content near the boundary very high. In the ESEM experiments, the moisture flux from the ambient humid air is maximized at the pore boundary as computed in fig. S4, allowing us to assume a high moisture content near the pore boundary.

As seen in fig. S3B, these two different models provide similar deformations. First of all, the radius of holes increases but the distance between adjacent pore boundaries decreases, which causes necking of the sheet between two pores that would lead to pore coalescence. The effective, von Mises stress (often used in failure criteria of materials) is localized near pores, particularly at the pore-pore interface, due to stress concentration. Notably, it is dominated by the positive (tensile) hoop stress (the stress component defined in the circumferential direction of pores) responsible for pore expansion. The rupture or cracking of pores is likely to be initiated by these highly tensile stress components particularly in the necking region between pores. These results clearly demonstrate that pore deformation characteristics in the two situations are similar, suggesting that our biaxial stretching experiment can closely emulate the pore coalescence phenomenon in the actual hygroscopic expansion of porous sheets.

section S3. Recovery of microporous structure of cellulose sponges

To test whether microporous structure of cellulose sponges is recovered after repeated cycles of wetting and drying, we took scanning electron microscopy (SEM) images of dry cellulose sponges that had undergone saturation and drying cycles with water. As shown in fig. S5, the microporous structures are similar regardless of the number of cycles of wetting and drying.

section S4. The volume fraction of aqueous liquid in a cellulose sheet

The volume fraction of an aqueous liquid in a cellulose sheet, η, is given by $\eta = V_l/V_c$, where V_l and V_c are the volumes of the liquid and the cellulose, respectively. In fig. S6a, we see that the cellulose volume $V_c = V_t - V_p$, where V_t and $V_p \sim N_0 r_0^2 s$ are the total volume and micropore volume, respectively. Since the porosity of the sheet $\phi = V_p/V_t$, we obtain $V_c \sim (1-\phi)N_0 r_0^2 s/\phi$.

The image analysis as illustrated in fig. S6b gives $\phi \approx 0.47$. The diffusion length $l_d \sim (Ds/u)^{1/2} \sim 0.1$ μm is very small compared to the micropore radius $r_0 \sim 1$ μm for the typical wicking velocity $u \sim 0.1$ mm/s in the late stages. Thus, we write $V_l \sim N_0 r_0 l_d$, which finally leads to $\eta \sim \phi l_d/(1-\phi)/r_0$.

section S5. Effects of water concentration on hygroscopic strain

In our experiments to induce hygroexpansion of sponges, we used not only water but also aqueous liquids, i.e. glycerin and ethylene glycol mixed with water at different weight ratios, to check the validity of our theory for a wide range of liquid properties, such as density, viscosity, and surface tension coefficient. We measured the maximum (or saturated) hygroscopic strain, ε_s of cellulose sponges for various aqueous liquids independently of the capillary rise experiments. The results, displayed in fig. S7, show that the values of ε_s for various liquids is nearly identical to the value for pure water when the weight content of water is over 20%. Thus, we use $\varepsilon_s = 0.23$ for all the liquids in this work, which leads to $\alpha \approx 0.33$.

section S6. Mechanical properties of cellulose sponges

We measured Young's modulus of the present cellulose sponges by using a tensile testing machine (Instron 5543). To obtain Young's modulus of the solid part except pores, we introduce a linearized empirical relationship (*36*), $E = E_0(1-\Phi)$ where E and E_0 are Young's modulus of porous material and solid part, respectively, and Φ is the macroscale bulk porosity ($\Phi \approx 0.9$). We use Poisson's ratio $\nu = 0.30$ following Ref. (*26*). The shear modulus is given by $G = E_0/(1+\nu)/2$. The elastic modulus decreases as the cellulose sponge absorbs water as shown in fig. S8. As the shear modulus of a wet porous medium appearing in the expression of diffusivity, we used $G = 1.62$ MPa.

section S7. Capillary rise in pre-swollen sponges

To test the effects of hygroscopic swelling on capillary rise dynamics, we measured the rise height of water in a sponge which had been swollen by water vapor without its micro and macro voids filled with the liquid. Figure S9 shows that the water rise height grows like $t^{1/4}$ in the late stages in pre-swollen sponges, while it grows like $t^{1/5}$ in unsaturated sponges. This result indicates the critical role of the hygroscopic swelling in the capillary rise dynamics in the late stages. The inset of fig. S9 shows that the power law of the rise height follows Lucas-Washburn's rule ($t^{1/2}$) regardless of liquids in the early stages.

section S8. Scaling laws of water rise within bread made from starch

Starch, the most common carbohydrate in human diets, is a polymeric carbohydrate that swells with absorbing water just as cellulose. To observe water wick against gravity in a bread made from starch, we placed an initially dry bread on a water bath as shown in fig. S10A. The measurement results of the rise height reveals that h grows like $t^{1/2}$ in the early stages and $t^{1/5}$ in the late stages, fig. S10C, which agrees with the power laws observed with cellulose sponges. Pores of bread were found to coalesce while impregnated with water as shown in fig. S10B, the similar behavior seen in the cellulose sponges.

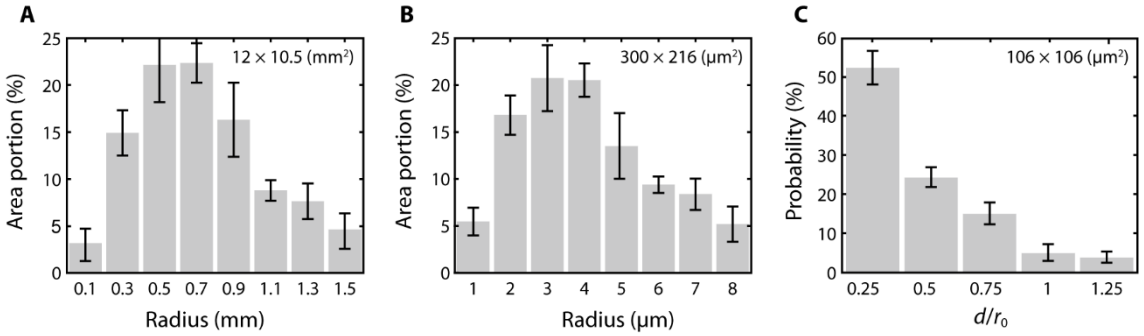

fig. S1. The measurement data of the cellulose sponge structure. (**A**) Optically measured areal density of macropores. (**B**) Areal density of micropores measured with SEM images. The error bars of the data correspond to the standard deviation of the average pore radii of three samples. (**C**) Inter-pore distance distribution of the cellulose sheets. The error bars of the data correspond to the standard deviation of the average inter-pore distance of six samples. The area of measurement is specified in each plot.

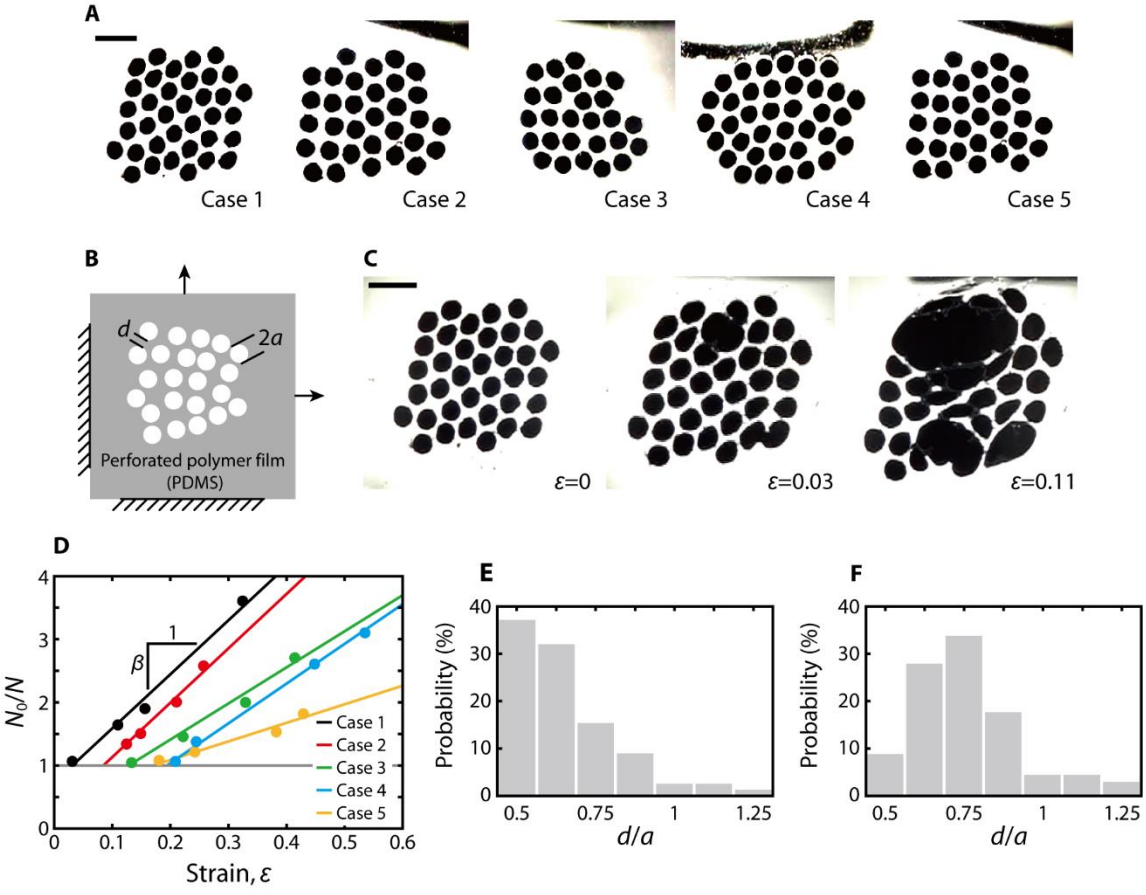

fig. S2. Macroscopic experiments for pore coalescence. (**A**) Perforated thin polymer films (initial state). The radius of pores, a, is 2 mm. Scale bar, 10 mm. (**B**) A schematic of experimental setup. The left and bottom sides are clamped, and the right and upper sides of the film are pulled by the linear stages. (**C**) Experimental images of the pore coalescence (case 1). Scale bar, 10 mm. (**D**) The number ratio N_0/N versus strain ε. The coalescence tends to occur quickly when β is high. Dimensionless inter-pore distance (d/a) distribution of case 1 (**E**) and case 5 (**F**).

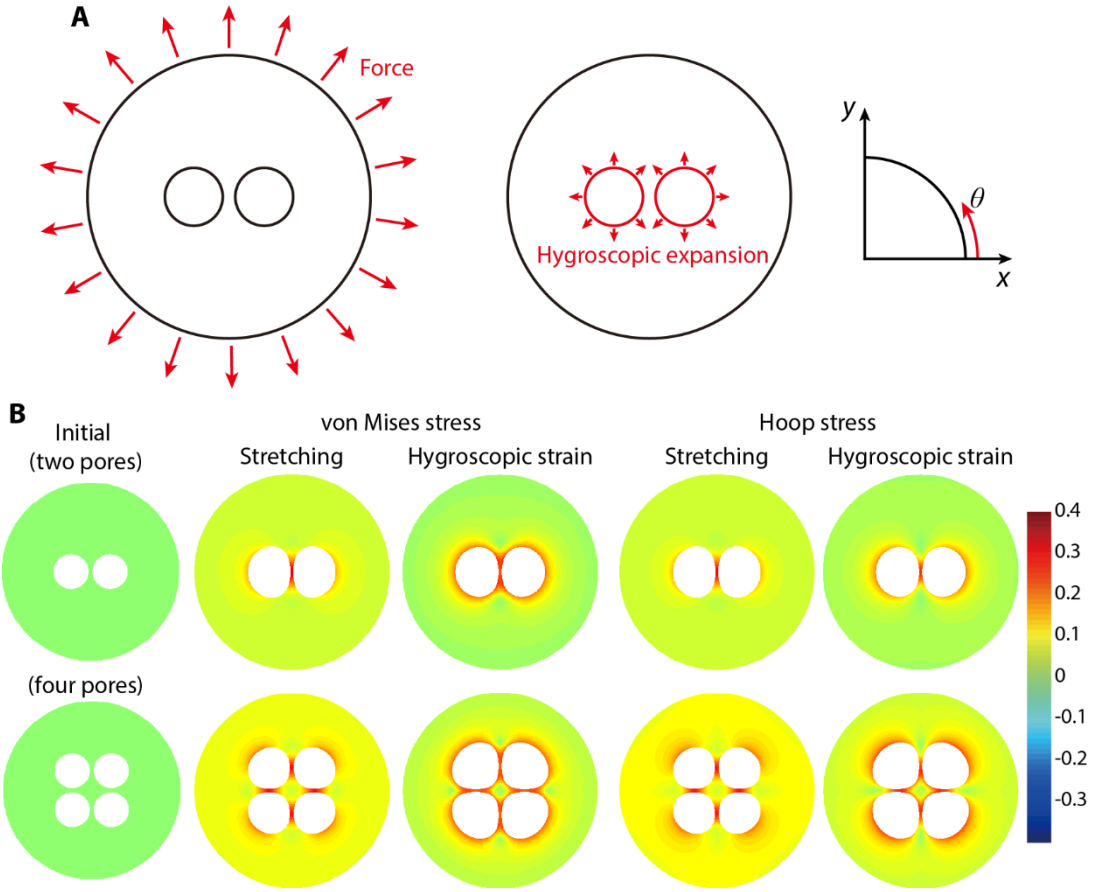

fig. S3. Numerical analysis of porous sheet deformation. (A) The loading conditions for finite element models. Left: external stretching. Right: hygroscopic swelling. (B) Von Mises stress and hoop stress distribution of stretching and hygroscopic swelling models. The hoop stress is defined by the stress along the θ-θ direction with the origin of cylindrical coordinate located at the center of individual pores. The color bar indicates the relative stress.

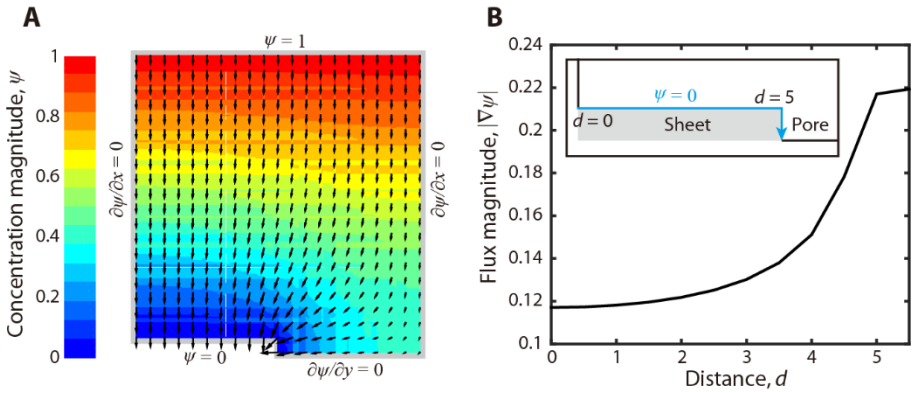

fig. S4. Moisture flux into cellulose sheet in ESEM chamber. (A) Numerical computation results of the moisture concentration (ψ) distribution based on the steady diffusion model, $\nabla^2\psi = 0$, with the boundary conditions specified in the figure. Black arrows indicate the orientation of the flux. (B) Flux magnitude versus distance along the blue line (inset). The flux is very high near the boundary between the sheet and the pore at $d = 5$.

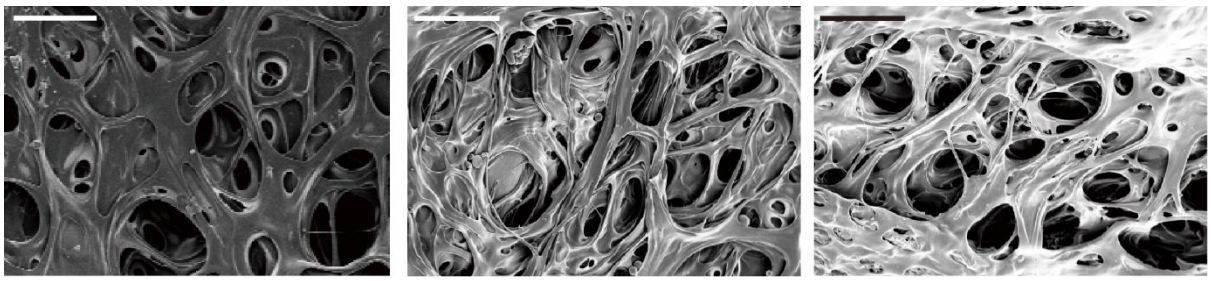

fig. S5. Microporous structure of cellulose sponges after cycles of wetting and drying with water. From left to right, SEM images of sponge after 0, 5, and 10 cycles. Similar microporous structure is observed although different specimens are used for microscopy due to experimental limits. Scale bar, 10 μm.

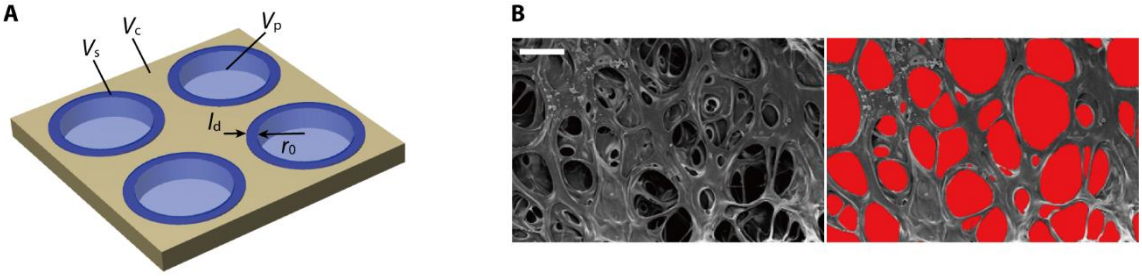

fig. S6. Analysis of the cellulose sheets. (**A**) A schematic of liquid diffusion in a wet microporous cellulose sheet. (**B**) SEM image (left) and post-processing image (right). We calculated the area fraction of pores (red area) to measure the porosity of a sheet. Scale bar, 10 μm.

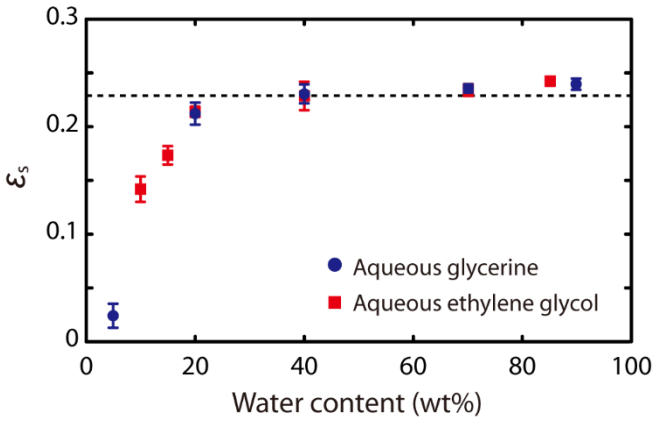

fig. S7. Hygroscopic strain of saturated sponge for different water contents in aqueous glycerin and ethylene glycol. The error bars of the data indicate the standard deviation of the average hygroscopic strain of four measurements at each weight concentration.

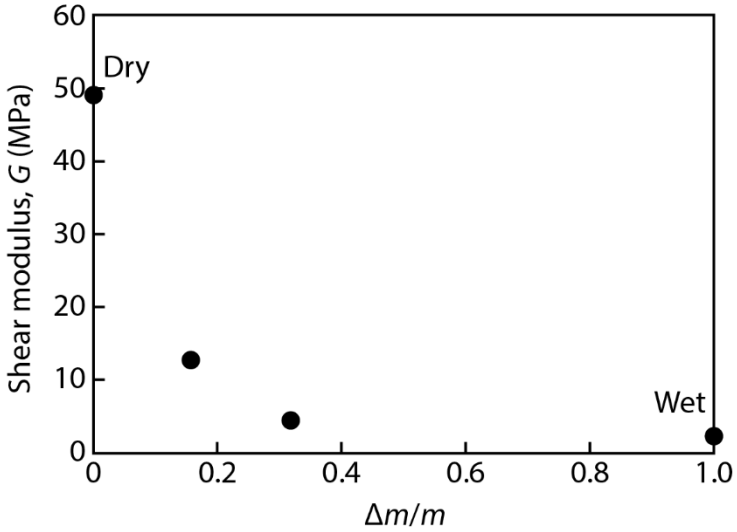

fig. S8. Shear modulus of dry and wet cellulose sponge. The shear modulus calculated from the measurement results of Young's modulus for different water concentration, $\Delta m/m$, where Δm is the mass of water and m is the mass of initially dry sponge. The error bar is smaller than the size of the symbols.

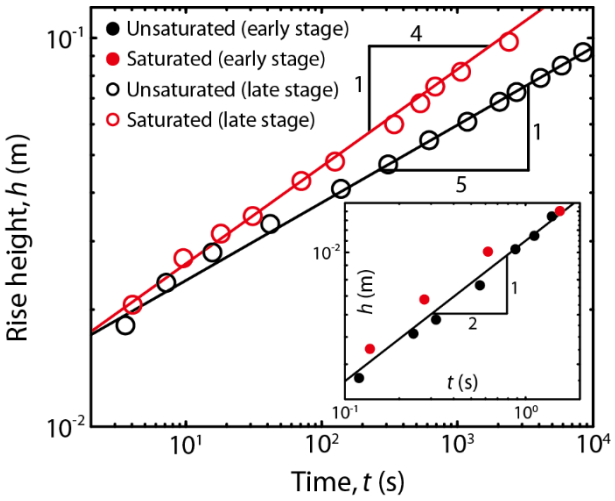

fig. S9. Capillary rise height of water versus time in an initially dry sponge (black) and pre-swollen sponge (red). In the late stages, the rise height grows like $t^{1/4}$ in the pre-swollen sponge while it follows the $t^{1/5}$ law in the initially dry sponge. Inset: In the early stages, the rise heights of the both saturated and unsaturated sponges follow the $t^{1/2}$ rule.

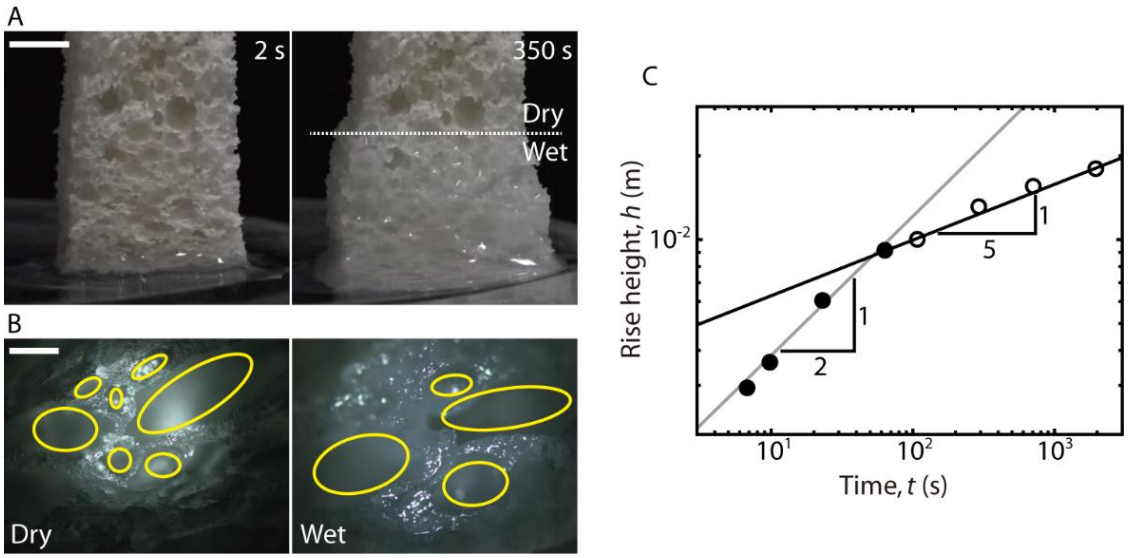

fig. S10. Capillary rise in porous bread. (**A**) Optical images of water wicking in initially dry bread. Scale bar, 5 mm (**B**) Merging of pores with water impregnation as imaged by an optical microscope. Scale bar, 30 μm. (**C**) The rise height of water versus time. In the early stages (filled symbols), the rise height grows like $t^{1/2}$ (gray line). In the late stages (open symbols), the rise height follows the $t^{1/5}$ rule (black line).

table S1. List of liquid properties and symbols. Physical properties of water, aqueous glycerin (*37*), aqueous ethylene glycol (*38*), turpentine and silicone oils at 23°C, and symbols for the liquids.

Liquid	Symbol		Viscosity, μ (Pa·s)	Density, ρ (kg/m^3)	Surface tension, γ (N/m)	Diffusivity, D (10^{-11} m^2/s)
	Early	Late				
Water	●	○	0.001	998	0.072	17.72
Glycerine 30 wt%	★	☆	0.0022	1071	0.069	8.05
Glycerine 60 wt%	◆	◇	0.009	1151	0.068	1.97
Glycerine 80 wt%	▲	△	0.047	1205	0.065	0.38
Ethylene glycol 30 wt%	▼	▽	0.0017	1033	0.061	10.43
Ethylene glycol 60 wt%	◀	◁	0.0038	1067	0.055	4.66
Ethylene glycol 80 wt%	▶	▷	0.0068	1090	0.050	2.61
Turpentine	■	□	0.0014	870	0.027	-
Ethylene glycol 99 wt%	×	-	0.018	1112	0.048	-
Silicone oil I	+	-	0.10	970	0.020	-
Silicone oil II	*	-	1.00	970	0.020	-

movie S1. Wicking and swelling in the cellulose sponge. The movie plays at 32X real-time speed. The cellulose sponge swells while being wetted.

movie S2. The merging of micropores in the cellulose sheets. The movie plays at 64X real-time speed. As the cellulose sheets absorb the water in the humid ESEM chamber, the pores expand, and then merge to form larger pores.